Positron annihilation spectroscopy and photoluminescence investigation of LaOF:Tb³⁺ nanophosphor fabricated via ultrasound assisted sonochemical route

C. Suresh [a,b], H. Nagabhushana [a,*], G.P. Darshan [c], R.B. Basavaraj [a], S.C. Sharma [d,e], D.V. Sunitha [f], B. Daruka Prasad [g]

[a] Prof. C.N.R. Rao Centre for Advanced Materials, Tumkur University, Tumkur 572 103, India
[b] Department of Physics, Government First Grade College, Tumkur 572 103, India
[c] Department of Physics, Acharya Institute of Graduate Studies, Bangalore 560 107, India
[d] Department of Mechanical Engineering Jain University, Advisor, Jain Group of Institutions, Bangalore 560069, India
[e] Advisor, Avinashilingam Institute for Home Science and Higher Education for Women University, Coimbatore 641 043, India
[f] School of Physics, Reva University, Bangalore 560064, India
[g] Department of Physics, BMS Institute of Technology and Management, VTU-affiliated, Bangalore 560 064, India

ARTICLE INFO

ABSTRACT

LaOF:Tb³⁺ nanophosphors were synthesized by modified sonochemical route using extracted Epigallocatechin gallate (EGCG) from green tea powder as surfactant. Powder X-ray diffraction patterns confirm the tetragonal phase of samples. Morphology of the products was tuned by changing the influential experimental parameters. Positron annihilation spectroscopy (PAS) was used to investigate the defect chemistry of the prepared samples. PAS specified the presence of defects at crystallite boundaries, vacancy clusters and large voids in the prepared compounds. Photoluminescence emission spectra consists of characteristic green emissions owing to $^5D_4 \rightarrow {}^7F_J$ (J = 6, 5, 4, 3) transitions of Tb³⁺ ions. The estimated critical distance between dopant ions was found to be ∼16.60 Å is majorly responsible for the dipole-dipole interaction and concentration quenching. The photometric study such as Commission Internationale de L'Eclairage, Correlated Color Temperature and Color purity indicates that the obtained phosphors could be a promising green component for optoelectronic applications in particular to white LEDs.

© 2017 Elsevier B.V. All rights reserved.

1. Introduction

In recent years, rare earth ions doped inorganic luminescent materials have fascinated due to their diverse potential applications namely white light-emitting diodes (WLEDs), sensors, biological imaging, field emission displays (FEDs), solar cells etc. [1–3]. The luminescent properties of Ln³⁺-doped phosphors are host independent due to the transitions of inner f-shell electrons [4,5]. Therefore, the selection of appropriate inorganic phosphors with efficient luminescent performance creates numerous interests for research community. Until now, some inorganic hosts, namely molybdates, oxides, fluorides, and silicate, were extensively investigated towards display device applications and were listed in Table 1 [6–15]. Among, fluorides LaOF possess low cut-off phonon

energy with decreasing the possibility of different non-radiative transition and thus leading to superior luminescent properties [16,17].

Further, during fabrication commonly occurred lattice defects such as voids or pores, clustered vacancies and mono vacancy greatly affected the luminescence. Positron annihilation spectroscopy (PAS) has been considered as new probe to illustrate surface defects and to understand the effect of size, quantum effects as well as surface defects of the nanomaterials, due to the better diffusion length of positrons as compared with crystallite size of the nanomaterial which makes restrictions on surface of the particles [18–21]. After thermal treatment, embedded positrons may diffuse in the medium followed by electron annihilation. High tendency of positrons induce defects in the material which results longer lifetime; therefore, longer positron life-times can be related with crystallite size and defect concentration [22–24].

Moreover, the Doppler broadening (DB) in the γ-spectrum was utilized to notice the particular type of defects, preserving and

---

Table 1
List of rare earth doped phosphors applicable to wLED's.

Phosphor	Excitation	Emission	CIE (X, Y)	CCT(K)	Refs.
$Bi_2O_3:Eu^{3+}(1.5\%):Tb^{3+}(0.5\%)$	374, 362, 322	590, 611, 623	(0.49, 0.34)	1830	Dimple et al. [6]
	322, 370, 380	486, 544, 584, 622	(0.31, 0.26)	7961	
			(0.27, 0.23)	32276	
$LaF_3:Tm,Eu,Tb$	378	541	(0.331, 0.332)	4991	Lorbeer et al. [7]
	355	449, 540	(0.317, 0.332)	6500	
		590	(0.312, 0.329)	3309	
$ZnO:Eu^{3+}$	394	590, 615, 648, 702	(0.501, 0.484)	–	Chandrashaker et al. [8]
$Mg_2SiO_4:Sm^{3+}$	315	576, 611, 656, 713	(0.588, 0.386)	1756	Naik et al. [9]
$Gd_{1.96-x}Y_xEu_{0.04}O_3$	305	611, 582, 641	(0.663, 0.328)	–	Shilpa et al. [10]
$Sr_3MgSi_2O_8:Eu^{2+}$	375	470, 570	(0.32, 0.33)	5892	Kim et al. [11]
$Sr_3Y_2(BO_3)_4:Dy^{3+}$	370	488, 575, 665	(0.2997, 0.3142)	5896	Li et al. [12]
$GdAl_3(BO_3)_4:Dy^+, Ce^{3+}$	400	480, 575, 620	(0.31, 0.33)	6480	Zhang et al. [13]
$Sr_3B_2O_6:Ce^{3+}, Eu^{2+}$	351	434, 574	(0.31, 0.24)	–	Chang et al. [14]
	395	505, 625	(0.35, 0.41)	5088	
$Sr_2SiO_4:Eu^{2+}$	400	550	(0.39, 0.41)	–	Park et al. [15]

reflecting the energy momentum distribution of an electron in the material [25–27]. Energy momentum distribution of an electron in a defect was quite different from the electrons momentum in the bulk material, therefore DB considered as a probe to identify the specific defects [28–30]. The vacancy defects are playing a vital role in changing the properties of material at nanosized. Many in appropriate efforts have been done to identify the modifications of properties by altering experimental parameters. Thus, positron lifetime and Doppler broadening accurately identifies the vacancy-type defects [31,32].

Lanthanide oxyfluoride (LaOF) was considered to be a novel host and having a wide range of applications due to their high ionicity, low phonon energy (550 cm^{-1}) [33], chemical stability etc. compared with those of fluorides and oxides [34–37]. Since the La^{3+} ions has the largest ionic radius among the lanthanide series, it can be easy substituted by different Ln^{3+} ions in the structure [38].

Up to now, many efforts have been made to fabricate LaOF nanophosphor, by diverse routes namely hydrothermal, sol–gel, solution combustion method, Co-precipitation, etc., [39–43]. However, these methods have several disadvantages such as large crystallite size, harsh reaction conditions and require sophisticated instrumentation, which rigorously obstruct their possible applications. Therefore, eco-friendly and cost effective fabrication route which produce LaOF nanophosphor with reproducible shapes and dimensions is highly desired [44]. The importance of choosing a proper synthetic route in designing nanostructured materials has been a driving force for the development of new methodologies for several decades. Indeed, this has led scientist's interest to the development of versatile and generalized synthetic methods readily adaptable for the preparation of a variety of nanostructured materials. Among a variety of approaches, the utilization of ultrasound for materials synthesis has been extensively examined over many years and is now positioned as one of the most powerful tools in nanostructured materials synthesis.

Compared to traditional energy sources, ultrasonic irradiation provides rather unusual reaction conditions (in a short duration; there is a formation of extremely high temperatures and pressures in liquids) that cannot be realized by other methods. Interestingly, such extraordinary conditions are not derived directly from ultrasound itself: acoustic wavelengths are much larger than molecular dimensions. Thus, no direct, molecular level interaction between ultrasound and the chemical species takes place. Instead, acoustic cavitation (i.e., the formation, growth, and implosive collapse of bubbles in liquids (Fig. 1)) driven by high intensity ultrasound accounts for the chemical effects [45]. When liquids are irradiated with ultrasound, the alternating expansive and compressive acoustic waves creates bubbles (i.e., cavities) and makes the bubbles

oscillate (Fig. 1). The oscillating bubbles can accumulate ultrasonic energy effectively while growing to a certain size (typically tens of mm). Under the right conditions, a bubble can overgrow and subsequently collapse, releasing the concentrated energy stored in the bubble within a very short time (with a heating and cooling rate of >10^{10} K s^{-1}). This cavitational implosion is much localized and transient with a temperature of ∼5000 K and a pressure of ∼10^3 bar [46].

Surfactants have established to be the best shape modifying agents for the fabrication of nanostructures which is mainly associated to the surface adsorption of surface active molecules on diverse crystal planes of nucleating centers helps in engineering their morphology. Various types of modifying agents have been used for shape controlled production of nanostructures. Epigallocatechin gallate (EGCG) is found to be one of the key constituent found in green tea and contains 30–40% of water soluble polyphenols. Due to polyphenolic structure, it serves major contribution to hydrogen bonding. This hydrogen bonding enables the capacity of binding strongly to polyphenols present in EGCG and forms a micro/superstructures [47]. Further, EGCG is the most effective reactant when reacting with major reactive oxygen species (ROS) and free radicals through mechanisms namely electron delocalization, formation of intramolecular hydrogen bonds and molecular structure reorganization [48].

A many research has been carried out on the luminescence properties of RE^{3+} doped LaOF nanophosphor varying rare earth concentration to achieve a superior luminescent media. But as per our literature survey, till date no work has been reported on the synthesis of LaOF:Tb^{3+} (1–5 mol%) nanophosphor by eco-friendly ultrasound assisted sonochemical route using EGCG extract as a surfactant. The process of formation and the mechanism for the formation of morphologies were investigated on the basis of structural information provided by electron microscopy analysis. From Positron annihilation spectroscopic (PAS) analysis, the presence of defects at crystallite boundaries, vacancy clusters and large voids in the prepared samples was discussed. An attempt was made for the first time to estimate Judd-Ofelt parameters of the prepared samples from the emission spectra along with the structural information. The PL behavior and the spectroscopic investigation of LaOF:Tb^{3+} (1–5 mol%) nanophosphor are discussed.

2. Experimental and characterization

The precursors used for the preparation of LaOF:Tb^{3+} (1–5 mol %) nanophosphor were in analytical grade (AR) and without further purification. The chemicals used in the present work are
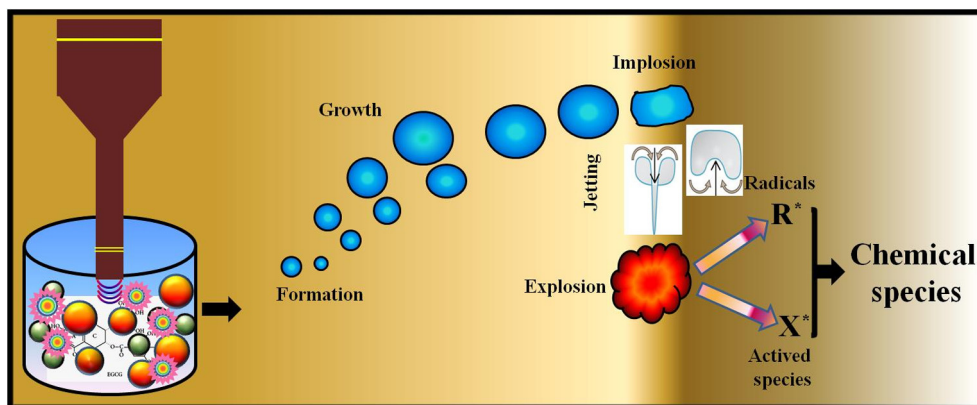
Fig. 1. Schematic representation of formation of LaOF: Tb^{3+} nanophosphor by ultrasound assisted sonochemical route.

Lanthanum nitrate [La(NO$_3$)$_3$·4H$_2$O (99.9%)], Ammonium fluoride [NH$_4$F; (99.9%)] and terbium nitrate pentahydrate [Tb(NO$_3$)$_3$·5H$_2$O (99.9%)] were procured from Sigma Aldrich. *EGCG* extract was used as a bio-surfactant. The stoichiometric quantities of Lanthanum nitrate and ammonium fluoride were dissolved in deionized water (50 ml) and mixed uniformly using magnetic stirrer for 20–25 min. The stoichiometric quantities of terbium nitrate pentahydrate (1–5 mol%) was added directly in the above solution. Further, 10 g of *EGCG* extract was well dissolved in 200 ml double distilled water and added slowly to the above obtained mixture (5, 10, 15, 20, 25 and 30 ml). The 72 mg NaOH well dissolved in 25 ml of water using magnetic stirrer. The resultant NaOH solution (0.1 mol%) was added to the reaction mixture in a drop wise at the rate of 2 ml/min to adjust the pH (1, 3, 5 and 9) value of the reaction solution. A titanium horn probe sonicator with ultrasonic frequency ~20 kHz, power ~300 W and sonication time ~1–6 h at a fixed temperature of 80 °C was introduced into the beaker containing resulting mixture. The precipitate obtained at the end of the reaction was filtered and washed several times using double distilled water and alcohol. The obtained powder was dried at 80 °C for 3 h in a hot air oven and then heat treated at ~700 °C for 3 h.

To analyze the structure of the prepared product, the powder X-ray diffraction (PXRD) measurements was performed on the Shimadzu made X ray diffractometer (Shimadzu 7000) with Cu-K$_\alpha$ radiation with nickel filter (λ = 0.15406 nm). Ni additional filter was used because Ni has high mass absorption coefficient which helps to have better monochromatic beam as compared to the graphite. The surface morphology of sample was studied by Hitachi made table top scanning electron microscope (Hitachi- TM 3000) and Transmission electron microscope (Hitachi H-8100, Kevex sigma TM Quasar, USA). The PerkinElmer Spectrophotometer (Lambda – 35) was utilized to study the diffuse reflectance (DR) spectra of the material. The Jobin YVON Horiba LABRAM-HR-Visible micro Raman system was used for Raman studies with He-Ne laser (~632.8 nm) as the source. The Spectroflourimeter equipped with Fluorolog-3 (Jobin Yvon) was utilized to measure the PL studies of the product. The PALS apparatus was a fast-fast coincidence spectrometer, with detectors consisting of a BC418 plastic scintillators (Saint-Gobain Crystals, Paris, France) coupled to a Burle 8850 photomultiplier tube (Burle Industries, Inc., Lancaster, PA). A 30 µCi ^{22}NaCl source was used for collecting spectra; the source was encapsulated in 8 µm Kapton foil. Coincidence Doppler broadening measurements were performed using two high pure germanium (HPGe) detectors having energy resolutions of 1.27 keV and 1.33 keV at 511 keV. PALSfit 3.0 software was used for the fitment of the data. This package used both the simple exponential decaying and also broadened decaying exponential functions to fit the lift time spectra.

3. Results and discussion

Fig. 2(a) shows PXRD patterns of pure and Tb^{3+} (1–5 mol%) doped LaOF nanophosphor (4 h ultrasound irradiation time, 30 ml of EGCG and pH ~9). All the diffraction peaks in the profile were well indexed to tetragonal phase of LaOF and matched with standard JCPDS. No. 89–5168. Further, no impurity peaks of dopant Tb^{3+} ions in the host were observed indicating that, the dopant ions were successfully substituted into the host lattice. In addition, the average crystallite sizes (D) and strain of nanophosphor was estimated using Scherrer's relation [49] and W-H plots (Fig. 2(b)) and values were listed in Table 2. Magnified view of a peak (1 0 1) and scheme to show estimation of crystallite size was shown in Fig. S1. As the concentration of Tb^{3+} ions in LaOF increases, the value of 'D' is also increases due to crystal distortion. It was evident the value of 'D' estimated from W-H plots is slightly lesser than those determined by Scherrer's relation. The small variation in the value of 'D' is owing to the fact that strain component in Scherrer's relation is considered to be zero.

Rietveld refinement method was used to confirm the tetragonal phase of the prepared samples using *FullProf suite* 3.00 program [50,51]. Various structural parameters namely Pseudo-Voigt profile function (u, v and w), isothermal temperature factors (B$_{iso}$), backgrounds scale factor, atomic coordinates etc., were evaluated [52]. The observed, calculated and the difference PXRD profiles of pure and LaOF: Tb^{3+} (1–5 mol%) nanophosphor was shown in Fig. S2(a–f). The experimental and calculated profiles showed nearly to zero in the intensity scale as illustrated by a line (Y$_{obs}$–Y$_{calc}$). The refined structural parameters of LaOF: Dy^{3+} (1–5 mol%) nanophosphor were summarized in Table 3. It was noticed that, a slight variation in structural parameters when the substitution of 8- coordinated Tb^{3+} ions to La^{3+} in LaOF. The packing diagram of tetragonal structured LaOF was drawn using the diamond software and was shown in Fig. S2(g).

The positron lifetime spectra of LaOF:Tb^{3+} (1 & 5 mol%) nanophosphor was shown in Fig. 3(a). It was evident that, in the beginning for the short interval, there is an increase in the counts indicates the increased positive ions later the decline of the positive ions lead to the creation of more vacancies in the prepared compounds. The positron lifetime and the corresponding intensities of LaOF: Tb^{3+} (1–5 mol%) nanophosphor was shown in Fig. 3 (b–e). The spectra exhibit two lifetime components (τ_1 and τ_2) with corresponding to intensities I$_1$ and I$_2$. The component τ_1 is shorter as compared to component τ_2 due to annihilation of positrons from grain and grain boundaries (Fig. 3(b & c)). After thermal treatment, the positron can travel a certain distance of ~50 nm and reaches grain boundary. Normally, the grain boundaries have enough defects which serve as strong trapping centers
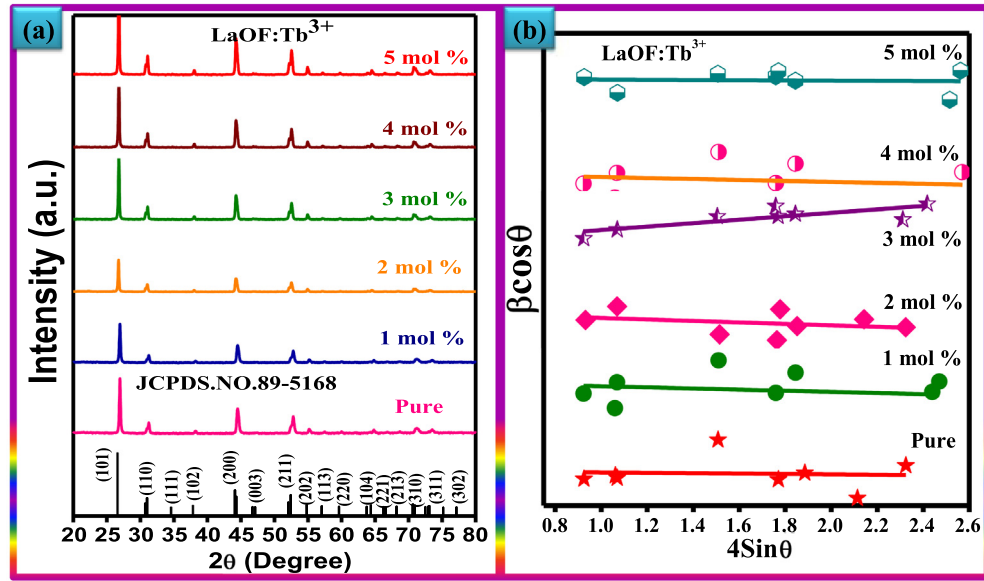
Fig. 2. (a) PXRD patterns and (b) W-H plots of pure and Tb^{3+} (1–5 mol%) doped LaOF nanophosphor.

Table 2
Estimated average crystallite size, strain and energy gap (E_g) of LaOF: Tb^{3+} (1–5 mol%) nanophosphor.

Tb^{3+} Conc. (mol%)	Crystallite size (D) (nm)		Strain (x 10^{-4})	E_g (eV)
	Scherrer's relation	W-H plots		
Pure	29.10	28.05	0.0444	5.88
1	29.42	28.38	0.0407	5.70
2	30.40	29.23	0.0527	5.81
3	30.57	29.90	0.0465	5.67
4	31.62	30.50	0.0426	5.78
5	31.86	30.12	0.0456	5.84

Table 3
Rietveld refined structural parameters of LaOF:Tb^{3+} (1–5 mol%) nanophosphor.

Structural parameters	Values/system for LaOF:Tb^{3+} (1–5 mol%) nanophosphor.					
Crystal system	Tetragonal					
Space group	P 4/n m m					
Hall symbol	P 4ab 2ab-1ab					
Lattice parameters (Å)	Pure	1 mol%	2 mol%	3 mol%	4 mol%	5 mol%
a = b	4.0819	4.0819	4.0885	4.0926	4.0928	4.0929
c	5.8215	5.8218	5.8289	5.8375	5.8378	5.8379
Unit cell volume (Å^3)	96.995	97.001	97.435	97.773	97.789	97.795
Results of rietveld refinement						
R_P	5.28	5.98	5.35	4.3	3.88	4.22
R_{WP}	6.65	7.55	7.07	5.73	5.23	5.72
R_{Exp}	11.0	11.0	9.59	7.74	7.46	7.41
$\chi2$	0.369	0.474	0.543	0.547	0.492	0.597
GoF	0.60	0.68	0.73	0.73	0.69	0.76
R_{Bragg}	4.39	7.24	7.09	2.25	2.18	2.81
R_F	3.21	4.82	4.86	2.20	2.16	2.53
X-ray density (g/cc^3)	5.955	5.954	5.928	5.907	5.906	5.906

for positrons. Therefore, a large number of positrons get trapped in the surrounding grain boundaries leads to few positrons to annihilate with free electrons inside the grain. If the positron lifetime in the grain boundary defects is close to their free annihilation lifetime in defect free region inside a grain, τ_1 represents a mixed lifetime containing both annihilation at grain boundary and mono vacancy in the crystallite. The intensity I_1 was found to be greater than I_2 (Fig. 3(d & e)) reveals that several positrons were annihilated at the grain and grain boundaries. Another lifetime component (τ_2) varies in the range of 1297 to 1324 ps due to positron

trapping at nano voids during annihilation time was shown in Fig. 3(c). The increased oxygen concentration due to trapping and annihilation of positrons in large vacancy clusters such as nano-voids lead to the increased positron lifetime (τ_2) [53]. The average positron lifetime (τ_{av}) of LaOF: Tb $^{3+}$ (1–5 mol%) nanophosphor was shown in Fig. 4(a). The variations in the τ_{av} value for different concentration of Tb^{3+} ions indicate that more number of cationic sites in host matrix. In addition, the average intensity (I_{av}) of the prepared sample was linearly decreases with increase of dopant Tb^{3+} concentration (Fig. 4(a)). The other parameters such as S and W
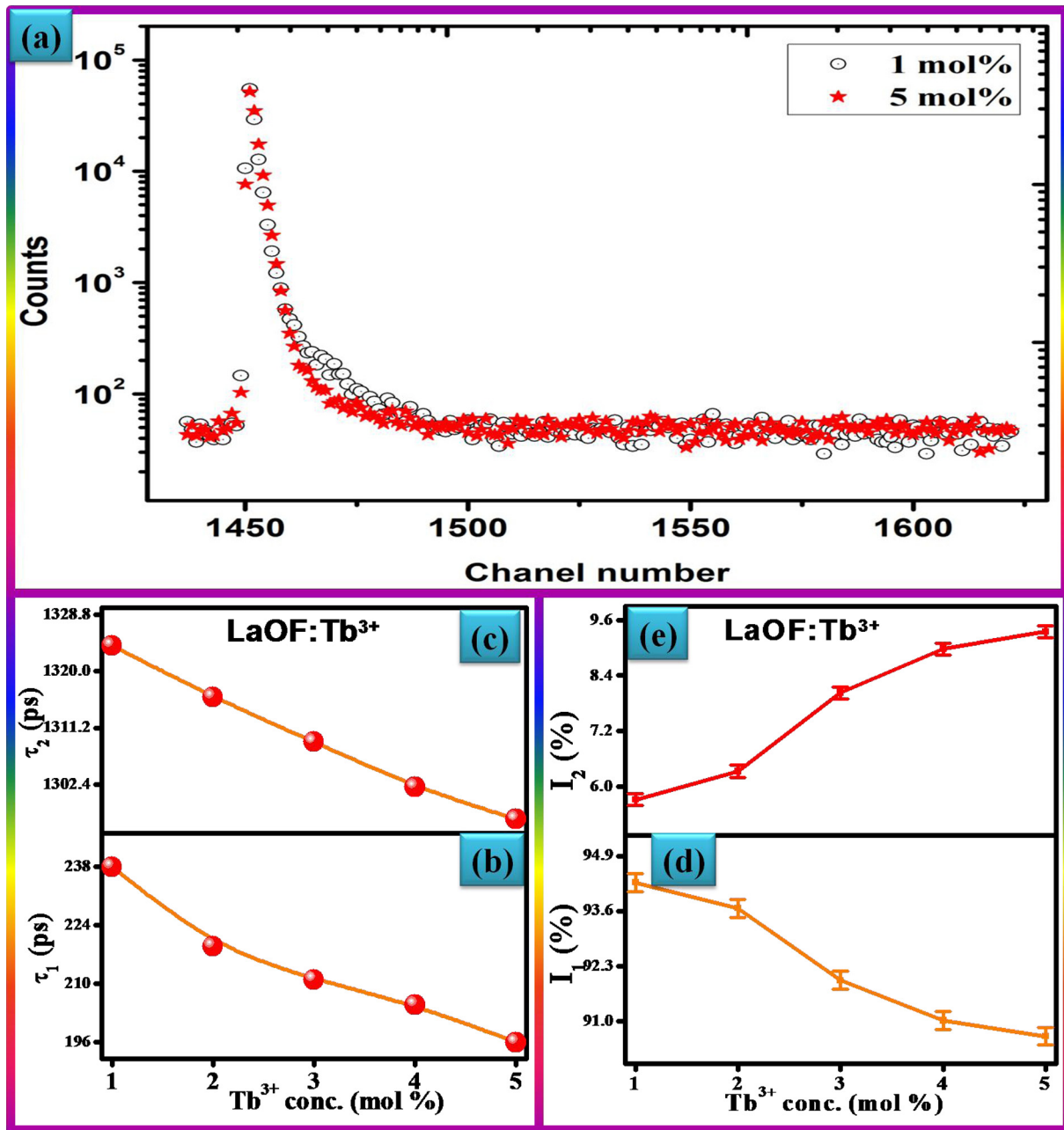
Fig. 3. (a) Peak-normalized positron lifetime spectra of doped LaOF:Tb^{3+} (1 & 5 mol%) nanophosphor, (b) The positron lifetimes τ_1, (c) τ_2 and corresponding intensities (d) I_1, (e) I_1 as a function of Tb^{3+} concentrations in LaOF nanophosphor.

can be derived from the positron DB spectroscopy clearly evident that the annihilation of positrons was due to valence and core electron respectively. The variation in S and W for different concentration of Tb^{3+} ions in LaOF host was also shown in Fig. 4(b). The value S decreases while parameter W increases with increase of Tb^{3+} concentration. The variation in the estimated crystallite size (D) for different concentration of Tb^{3+} ions was shown in Fig. 4(c). It was evident that, the value D increases with increases of Tb^{3+} ions concentration in LaOF host. It was observed that the estimated values of D were too small to avoid positrons diffuse out from surfaces and getting annihilated.

The S-W plot (Fig. 5(a)) exhibit a linear relationship indicating that the defect clusters that trap positrons basically remain of the same origin and configuration. It means that, the contribution

of surfaces to annihilation properties of the positrons was very less and other positron trapping defects such as dislocations were practically absent in the prepared samples. The variation of τ_{av} and S parameter as a function of estimated value of D was shown in Fig. 5(b). The τ_{av} and S-parameter was linearly decreases as a crystalline size increases. The estimated results from Positron annihilation lifetime studies (PALS) and coincidence Doppler broadening spectroscopy (CDBS) of LaOF:Tb^{3+} (1–5 mol%) nanophosphor were presented in Table 4.

The diffuse reflectance (DR) spectra of pure and LaOF:Tb^{3+} (1–5 mol%) nanophosphor recorded in the range 200–1100 nm at RT (Fig. 6(a)). A strong band in the range 200–350 nm was observed in the DR spectra due to band gap of present sample. Further, a weak absorption bands due to the meta-stable energy states
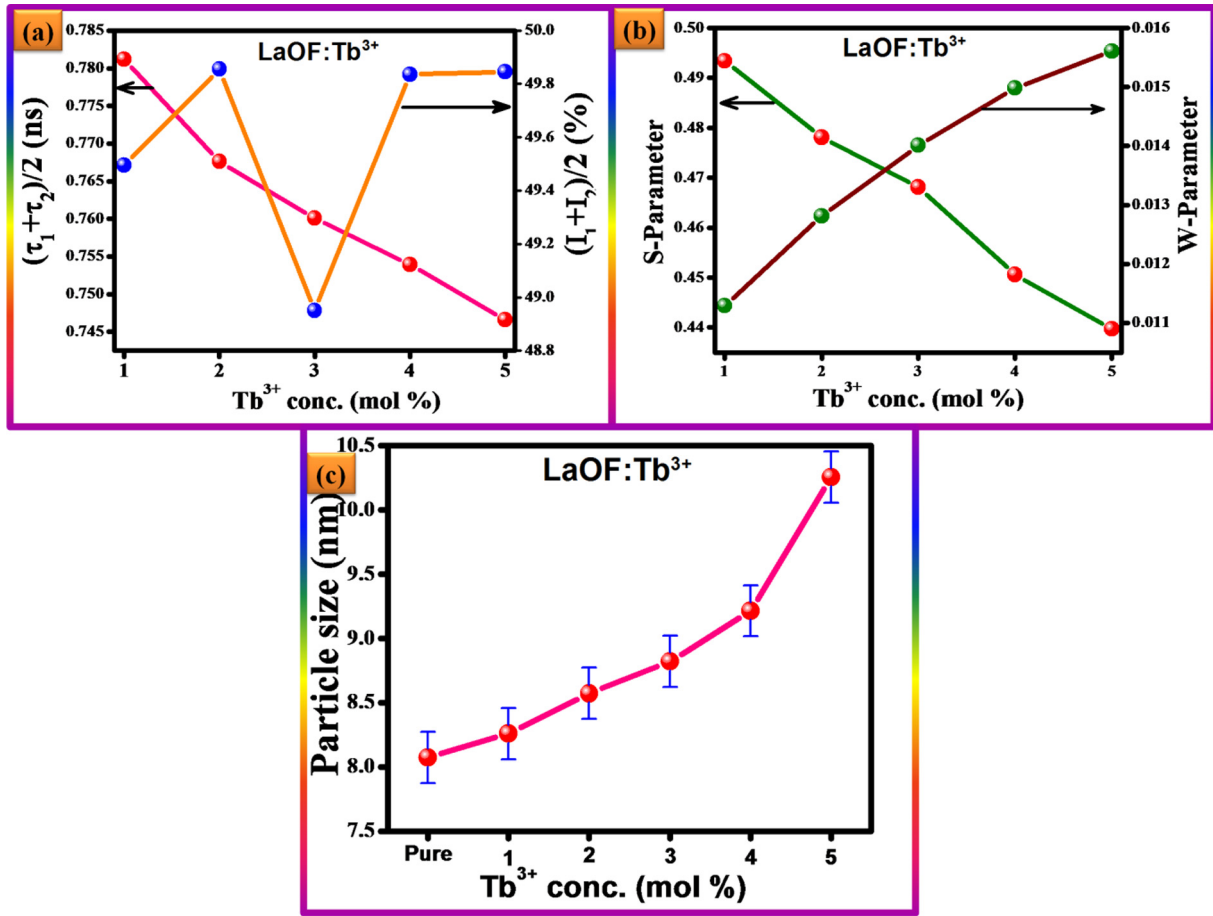
Fig. 4. (a) The average lifetime and corresponding average intensity, (b) plot of S and W parameters and (c) estimated crystallite size as a function of Tb^{3+} (1–5 mol%) concentration in LaOF nanophosphor.
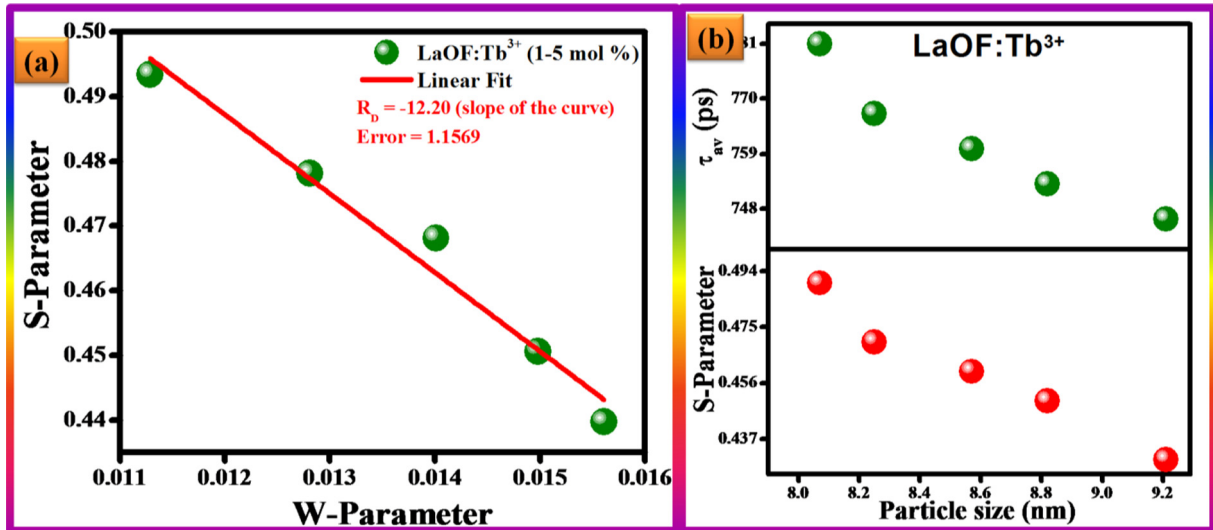

Fig. 5. (a) Plot of S v/s W parameter and (b) S-parameter and average positron lifetime (τ_{av}) as a function of particle size of the prepared LaOF:Tb^{3+} nanophosphor.

formed between the valence band and conduction band by the dopant Tb^{3+} ions are feebly visible in the spectra. This is because of the more band to band absorption of the host [54].

Kubelka–Munk theory was used to estimate the energy band gap (E_g) from DR spectra, [55]. The ratio of the light scattered from a thick layer of powder material and an ideal non-absorbing reference sample was recorded with respect to the wavelength λ [56]:

$$R_\infty = R_{sample} / R_{reference} \qquad (1)$$

Table 4
Positron annihilation lifetime studies (PALS) and coincidence Doppler broadening spectroscopy (CDBS) results of LaOF:Tb^{3+} (1–5 mol%) nanophosphor.

Tb^{3+} Conc. (mol%)	PAS				CDBS	
	$\tau_1 \pm 0.0016$ (ns)	$\tau_2 \pm 0.00151$ (ns)	$I_1 \pm 0.21$ (%)	$I_2 \pm 0.13$ (%)	S parameter $\pm$ 0.0016	W parameter $\pm$ 0.0004
1	0.238	1.3245	94.28	5.72	0.4934	0.01129
2	0.219	1.3163	93.67	6.33	0.4781	0.01281
3	0.211	1.3092	91.97	8.03	0.4687	0.01401
4	0.205	1.3028	91.02	8.98	0.4506	0.01498
5	0.196	1.2972	90.65	9.35	0.4397	0.01561
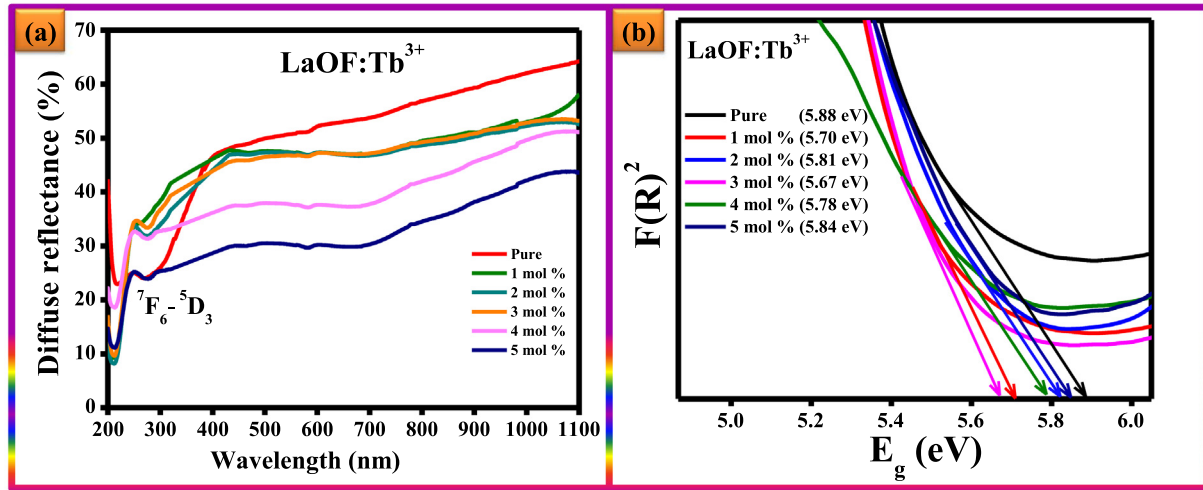
Fig. 6. (a) DR spectra and (b) energy band gap of LaOF:Tb^{3+} (1–5 mol%) nanophosphor.

The Kubelka–Munk function $F(R_\infty)$ relay the diffuse reflectance of the sample (R_∞), absorption coefficient (K) and scattering coefficient (S) and was specified by the relation [57]:

$$F(R_\infty) = \frac{(1-R_\infty)^2}{2R_\infty} = \frac{K}{S} \tag{2}$$

The E_g and linear absorption coefficient (α) of a sample was associated with the well-known Wood - Tauc relation:

$$\alpha h\nu = C_1(h\nu - E_g)^{1/2} \tag{3}$$

where $h\nu$; the photon energy and C_1; proportionality constant. When the powder sample scatters in completely diffuse behavior (or when it was illuminated at 60° incidence), the absorption coefficient (K) becomes equal to 2α. Considering the scattering co-efficient (S) as constant with respect to wavelength, and using Eqs. (4) and (5), the following relation can be expressed:

$$[F(R_\infty)h\nu]^2 = C_2(h\nu - E_g) \tag{4}$$

From the plot of $[F(R)]^2$ versus E_g as shown in the Fig. 6(b), the value of E_g was obtained by extrapolating the linear fitted regions to $[F(R_\infty)]^2 = 0$. The estimated values of E_g from the DR spectra using K–M function were tabulated in Table 2.

Fig. 7(a & b) shows the SEM micrographs of prepared samples. Form the figure, it evident that particles with dumbbell structure were observed. TEM images of LaOF: Tb^{3+} (2 mol%) nanophosphor was shown Fig. 7(c & d). Spherical shaped morphology of the product was observed. The average particles size was estimated using imageJ 1.46 R software was found to be ∼35 nm, which was in good agreement with results obtained from the PXRD. Fig. 7(e) shows the HRTEM image of optimal nanophosphor. It shows that the obtained product was highly crystalline in nature and interplanar spacing (d) was estimated and found to be ∼0.334 nm corresponding to (1 0 1) plane. The selected area electron diffraction

(SAED) pattern of prepared LaOF: Tb^{3+} (2 mol%) nanophosphor was shown in Fig. 7(f). The diffraction rings observed in pattern denotes the high crystallinity of the product and was well indexed to (1 0 1), (1 1 0), (2 1 1), (2 0 0) and (1 0 2) planes and good agreement with tetragonal phase of the prepared nanophosphor.

Fig. 8(a) shows the PL excitation spectrum of LaOF:Tb^{3+} (2 mol%) nanophosphor under ∼541 nm emission wavelength. The spectrum consists of a peak at ∼316, 360, 376 and 394 nm were attributed to $^7F_0 \rightarrow {}^5H_3$, $^7F_0 \rightarrow {}^5D_4$, $^7F_0 \rightarrow {}^5L_7$ and $^7F_0 \rightarrow {}^5L_7$ intra-4f transitions of Tb^{3+} ions respectively. Among the excitation peaks, a high intensity peak ∼376 nm is well matched with the wavelength of commercial NUV- LED chip, which signifying that the phosphors can be successfully pumped by NUVlight. The PL emission spectra of LaOF: Tb^{3+} (1–5 mol%) nanophosphor upon 376 nm excitation wavelength was shown in Fig. 8(b). The spectra comprised of a sharp emission peaks at ∼487, 541, 586 and 621 nm were due to $^5D_4 \rightarrow {}^7F_6$, $^5D_4 \rightarrow {}^7F_5$, $^5D_4 \rightarrow {}^7F_4$ and $^5D_4 \rightarrow {}^7F_3$ transitions of Tb^{3+} ions respectively [58].

Asymmetry ratio (A_{21}) between the emission peaks at ∼487 and 541 nm was estimated by following equation [59]:

$$A_{21} = \frac{\int_{535}^{560} A_2 d\lambda}{\int_{475}^{510} A_1 d\lambda} \tag{5}$$

where, subscript '1' and '2'; transitions of $^5D_4 \rightarrow {}^7F_6$ and $^5D_4 \rightarrow {}^7F_5$ respectively. The estimated values of A_{21} were listed in Table 4. The value of A_{21} in LaOF: Tb^{3+} (1–5 mol%) nanophosphor was increases linearly with increase of dopant concentration (Fig. 8(c)). It was evident that, with increase Tb^{3+} ions concentration leads to higher distortion in the host matrix. In order to know the optimum concentration of dopant Tb^{3+} ions in the host, PL emission intensity as a function of dopant concentration was plotted under at ∼376 nm excitation wavelengths (Fig. 8(c)). It was evident that,
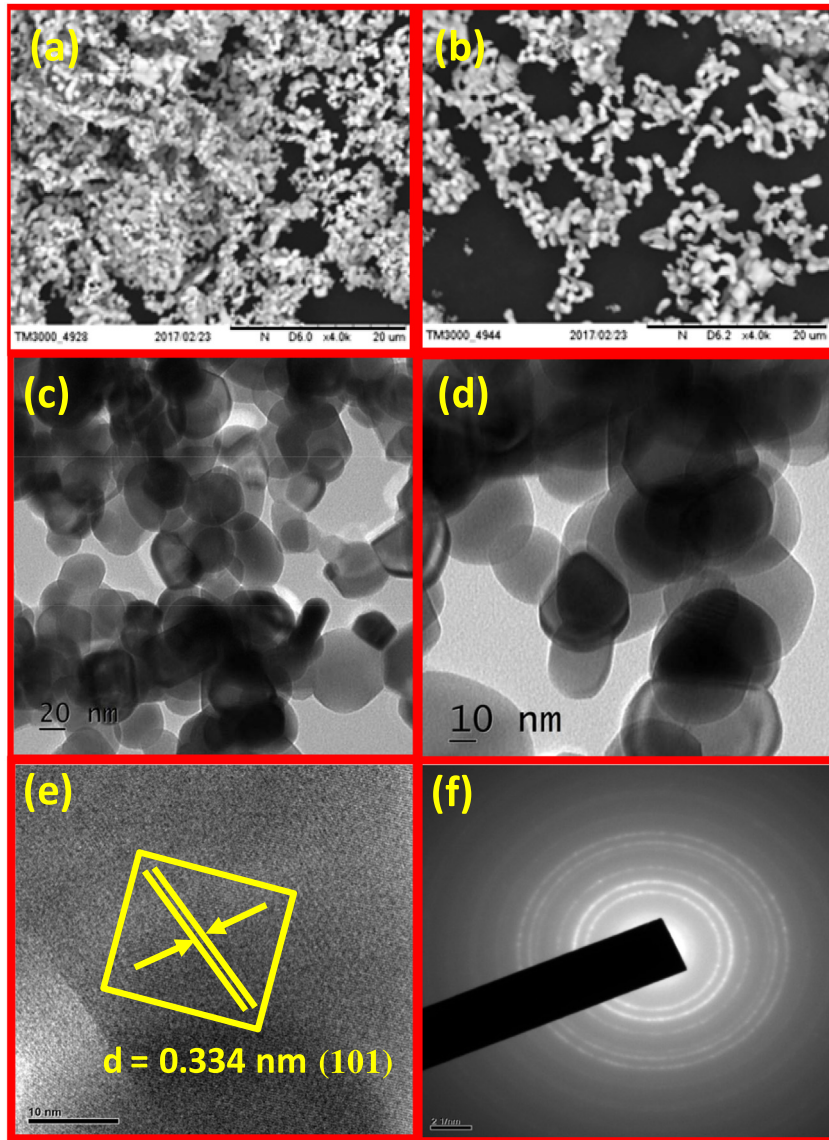
Fig. 7. (a & b) SEM, (c & d) TEM, (e) HRTEM image and (f) SAED patterns of LaOF: Tb^{3+} (2 mol%) nanophosphor.

PL emission intensity increases up to 2 mol% of Tb^{3+} ions and afterwards diminishes owing to concentration quenching.

Further, to know more about the concentration quenching phenomena, it was very significant to explore the interaction behavior, which usually takes place due to radiation re-absorption, exchange interactions and electric multipolar interaction. In view of this, critical distance between two adjacent dopant Tb^{3+} ions was estimated by using well known Blasse relation [60]:

$$R_c = 2(3V/4\pi NX_c)^{1/3} \tag{6}$$

where V; unit cell volume (97.435 $Å^3$), N; number of cations per unit cell ($N = 4$) and X_c; optimal concentration of Tb^{3+} ions (0.02). The estimated value of R_c was found to be ∼13.26 Å and was higher than 5 Å. It implies that the exchange interaction was not responsible for energy transfer among Tb^{3+} ions. Therefore, the non-radiative energy transfer takes place only due to multipole – multipole interaction. As per Van Uitert's report, the multipolar interaction occurring can be determined on the basis of change in the emission intensity from the emitting level [61] which follows from the Eq. (9):

$$\frac{I}{x} = \frac{K}{\beta(x)^{\frac{Q}{3}}} \tag{7}$$

where I/x; the emission intensity (I) per activator ion (x) of the phosphor corresponding to the dopant concentration x ($\geq x_c$), Q; the interaction type between the activator ions having values 6, 8 and 10 indicating exchange interactions, dipole–dipole (d–d), dipole–quadrupole (d–q) and quadrupole–quadrupole (q–q) interactions, respectively. K and β; the constants [61,62]. A plot of log (I/x) vs log (x) provided slope ($-Q/3$) value to be -1.365 after fitting the linear curve as shown in Fig. 8(d). The value Q was estimated to be 6.43 which is rounded to the nearest theoretical value of 6 for the dipole–dipole (d–d) interaction. This entails that d–d interaction is the main interaction mechanism for concentration quenching in the present phosphor.

To better understanding of the PL processes, the simplified energy level diagram of Tb^{3+} ions in LaOF host was shown in Fig. 9(a). Under 376 nm excitation, the electrons excited from the ground state ($^7F_6$) to the excited state ($^5G_6$). These excited electrons undergo non-radiative transition from excited state ($^5G_6$) to meta-stable state ($^5D_3$), resulting population inversion was achieved in the metastable state ($^5D_3$). Consequently, the second non-radiative transition happened and the electrons were decayed from $^5D_3$ level to the $^5D_4$ level. Finally, the electrons in the $^5D_4$ level undergo radiative transitions ($^5D_4 \rightarrow {}^7F_6$ at 487 nm, $^5D_4 \rightarrow {}^7F_5$ at
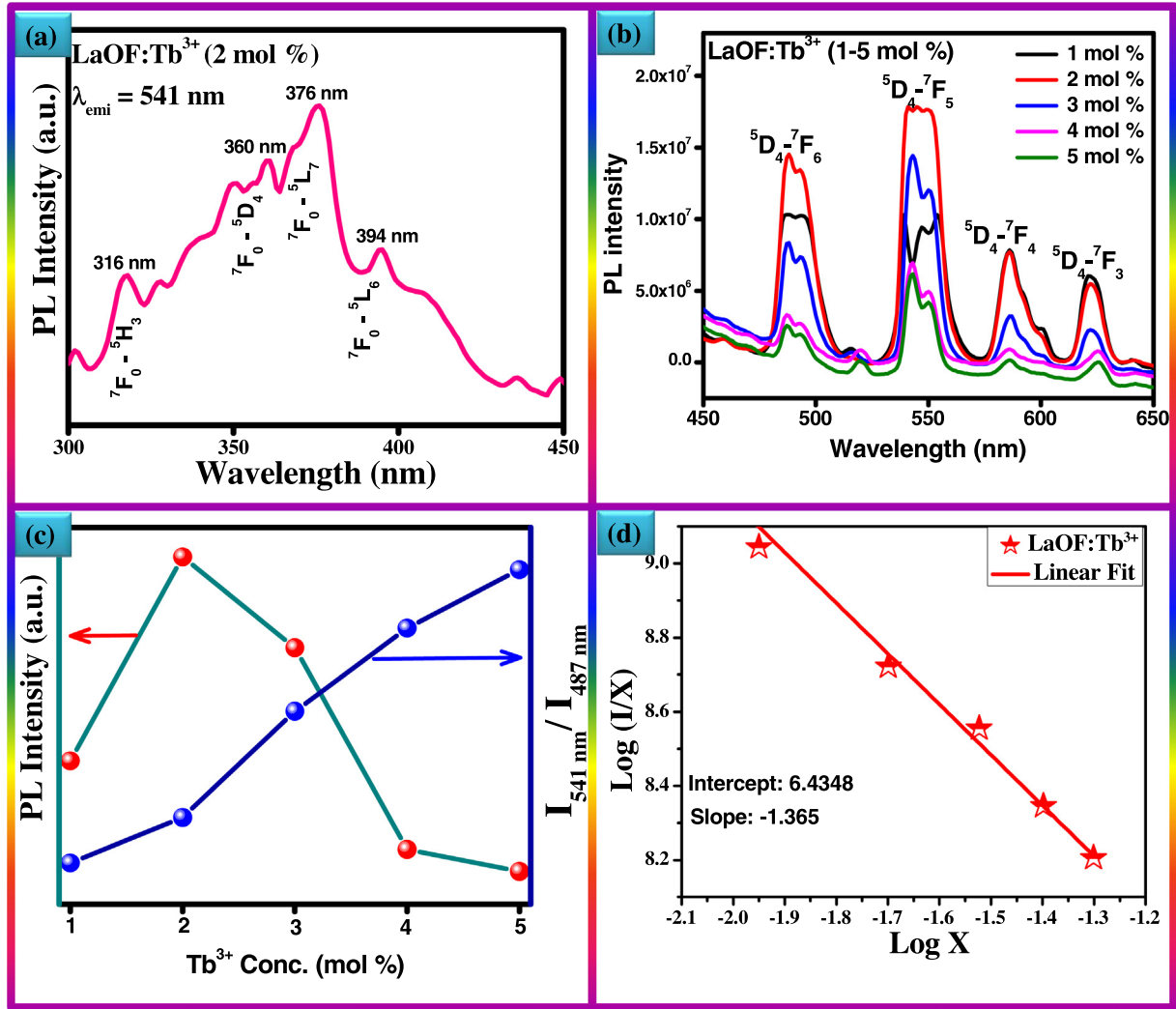
Fig. 8. (a) Excitation spectrum, (b) emission spectra, (c) variation of asymmetric ratio and PL intensity as a function of Tb^{3+} ions concentration (d) Logarithmic plot of (x) versus (I/x) in an LaOF: Tb^{3+} (1–5 mol%) nanophosphor.

541 nm, $^5D_4 \rightarrow {}^7F_4$ at 586 nm, and $^5D_4 \rightarrow {}^7F_3$ at 621 nm), leads to characteristic emissions of Tb^{3+} ions.

The Judd-Ofelt (J–O) intensity parameters (Ω_2 & Ω_4) and various radiative properties including radiative transition probability (A_T), radiative lifetime (τ_{rad}), and branching ratio (β_R) were estimated in order to know the site symmetry and PL dynamics of Tb^{3+} ions in LaOF matrix [63–64]. Although, J–O analysis was a powerful tool, which efficiently defines the spectral behavior in a specific co-ordination location of rare earth ions incorporated in single and polycrystalline materials, glasses and solutions. The relation between integrated emission and the radiative emission rates intensities were estimated by the relations as per literature [65].

$$\frac{A_{0-5,4}}{A_{0-6}} = \frac{I_{0-5,4}}{I_{0-6}} \frac{h\nu_{0-6}}{h\nu_{0-5,4}} \qquad (8)$$

where, A_{0-J}: radiative emission rates, I_{0-J}: integrated emission intensities (area under the PL peaks) and $h\nu_{0-J}$: energy corresponding to transition $^5D_4 \rightarrow {}^7F_J$ (J = 6, 5, 4). The radiative emission rates due to forced electric dipole transitions ($A_{0-5, 4}$) associated with J–O parameters can be estimated as follows.

$$A_{0-J} = \frac{64\pi^4(\nu_{0-5,4})^3 e^2}{3hc^3} \frac{1}{4\pi\varepsilon_0} \chi \sum_{J=6,5,4} \Omega_J \left\langle {}^5D_4|U^{(J)}|{}^7F_{5,4} \right\rangle^2 \qquad (9)$$

where χ; the Lorentz local field correction factor, and is connected with the refractive index (n) of the host via the equation $\chi = n(n^2 + 2)^2/9$. The non-zero square reduced matrix elements are taken from the references as: $\langle {}^5D_4|U^{(J)}|{}^7F_5\rangle = 0.0010$ and $\langle {}^5D_4|U^{(J)}|{}^7F_4\rangle = 0.0008$. Using Eqs. (8) and (9) the values of $\Omega_{2, 4}$ were estimated and listed in a Table 5.

The radiative properties namely radiative transition probabilities (A_T), radiative lifetimes (τ_{rad}) and branching ratios (β_R) for the excited states of Tb^{3+} were estimated using J–O parameters given by the following relations [66].

$$A_T = \sum_{J'} A_{J-J'} \qquad (10)$$

$$\tau_{rad} = \frac{1}{A_T(\psi_J)} \qquad (11)$$

$$\beta_R = \frac{A(\psi_J, \psi_J')}{A_T(\psi_J)} \qquad (12)$$

The estimated values were tabulated in Table 5. The calculated Ω_2 is more sensitive to the ligand environment, which can be clearly implicit by the most important change of its value with different concentrations of Tb^{3+} ions. The parameter, Ω_2, displays the
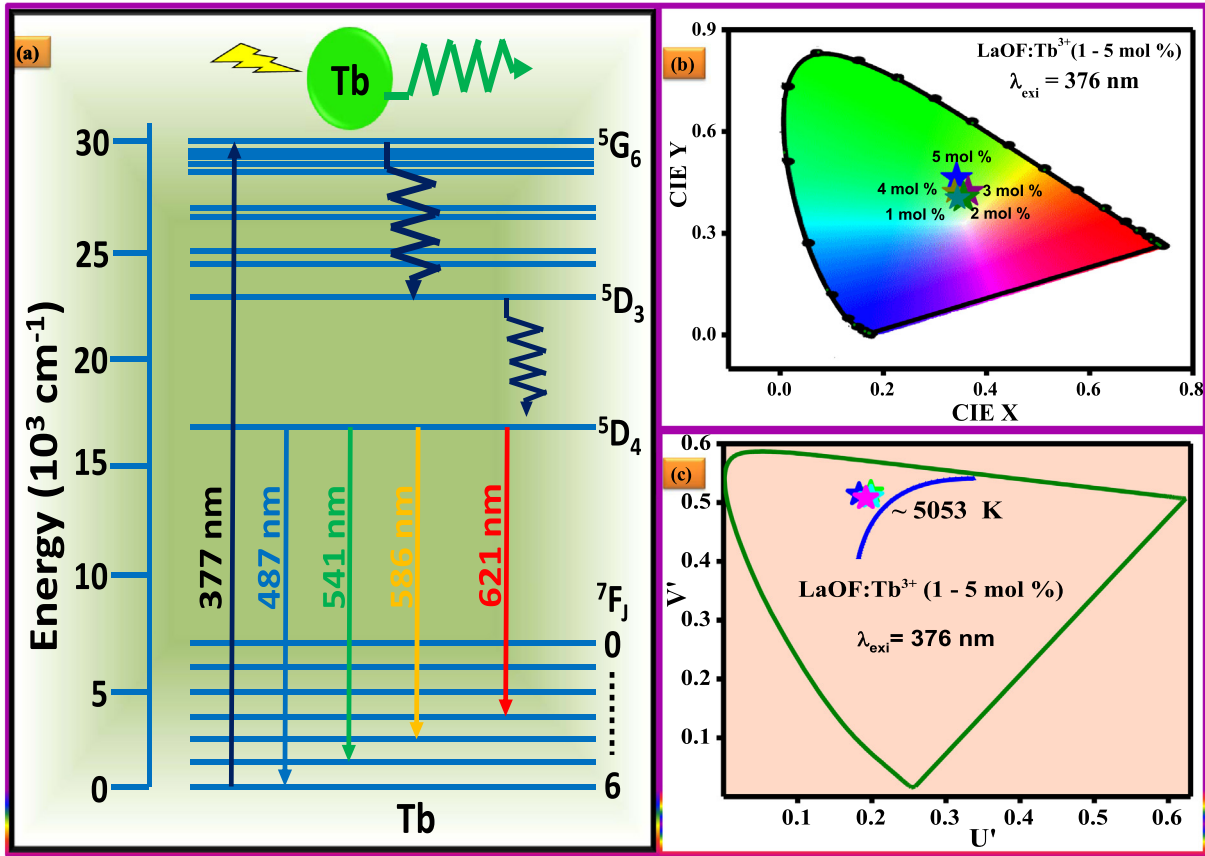
Fig. 9. (a) Energy level diagram showing the excitation and emission mechanism, (b) CIE and (c) CCT diagrams of LaOF: Tb^{3+} (1–5 mol%) nanophosphor.

Table 5
Judd-Ofelt intensity parameters (Ω_2, Ω_4), Emission peak wavelengths (λ_p in nm), radiative transition probability (A_T), calculated radiative (τ_{rad}) lifetime, branching ratio (β_R), asymmetric ratio (A_{21}) and quantum efficiency (η) of LaOF: Tb^{3+} (1–5 mol%) nanophosphor.

Conc. (mol%)	Judd-Ofelt intensity parameters ($\times 10^{-2}$ °cm²)		Emission peak wavelength λ_p in nm	A_T (s⁻¹)	τ_{rad} (ms)	β_R (%)	A_{21}	η (%)
	Ω_2	Ω_4						
1	6.85	0.96	541	54.19	16.47	0.93	1.27	60.71
2	6.91	1.23	541	56.64	16.51	0.92	1.30	65.24
3	7.32	1.64	542	52.33	17.73	0.94	1.33	48.52
4	7.48	2.32	541	50.84	17.02	0.92	1.45	42.56
5	7.23	1.89	541	51.82	16.76	0.94	1.42	41.85

dependence on the covalence between rare earth ions and ligands anions since Ω_2 replicates the asymmetry of the local environment at the Tb^{3+} ion site. The branching ratio is a critical parameter for the laser designer because it characterizes the possibility of attaining stimulated emission on any specific transition. The branching ratios are also used to predict the relative intensities of all emission transitions originating from a given excited state. It is known that a transition having branching ratio of ≥ 0.50 can emit laser radiation more effectively. The calculated branching ratio (β) of the optimized phosphor was found to be higher than 0.50, therefore present phosphor was potentially useful in color displaying devises [67].

By using Commission Internationale de L'Eclairage (CIE) co-ordinates, the color perception of human eye was expressed. Generally, the emission color of any material can be represented by chromaticity co-ordinates (x, y) [68]. The CIE co-ordinates of LaOF: Tb^{3+} (1–5 mol%) nanophosphor were estimated using PL

emission spectra and the values were listed in Table 6. The CIE chromaticity diagram of fabricated samples was shown in Fig. 9 (b). It was clearly evident from the figure that, the CIE co-ordinates were located in green region.

Coordinated color temperature (CCT) can be estimated by Planckian locus, which is only a small portion of the (x, y) chromaticity diagram and there exist many operating points outside the Planckian locus. If the coordinates of a light source do not fall on the Planckian locus, the CCT is used to define the color temperature of a light source. CCT is calculated by transforming the (x, y) coordinates of the light source to (u_0, v_0) by using the equations [69].

$$u' = \frac{4x}{-2x + 12y + 3} \tag{13}$$

$$v' = \frac{9y}{-2x + 12y + 3} \tag{14}$$

Table 6
Photometric characteristics of LaOF:Tb^{3+} (1–5 mol%) nanophosphor.

Tb^{3+} (mol%)	CIE		CCT (K)	CP (%)
	x	y		
1	0.3421	0.4627	5271	88
2	0.3643	0.4216	4647	92
3	0.3376	0.4220	5355	83
4	0.3555	0.4048	4823	81
5	0.3434	0.4033	5166	78

$$CCT(x,y) = -449n^3 + 3525n^2 - 6823.3n + 5520.33 \qquad (15)$$

where n = (x − 0.3320)/(y − 0.1858). By determining the temperature of the closest point of the Planckian locus to the light source on the (u$_0$, v$_0$) uniform chromaticity diagram and is shown in Fig. 9(c). The lamps with a CCT value below 3200 K are usually considered as 'warm' light sources, while those with a CCT above 4000 K are considered as 'cool' in appearance [49]. The CCT values of LaOF: Tb^{3+} (1–5 mol%) nanophosphor were calculated and listed in Table 6.

In addition, the quantum efficiency (η) of LaOF: Tb^{3+} (1–5 mol %) nanophosphor was estimated by using the relation reported elsewhere [70]. The calculated value of η tabulated in a Table 5. To know the practicability of the phosphor, color purities of the prepared LaOF: Tb^{3+} (1–5 mol%) nanophosphor were calculated by using the relation [71]:

$$Color\ purity = \frac{\sqrt{(x_s - x_i)^2 + (y_s - y_i)^2}}{\sqrt{(x_d - x_i)^2 + (y_d - y_i)^2}} \times 100\% \qquad (16)$$

where (x_s, y_s); the coordinates of a sample point, $(x_d = 0.21, y_d = 0.71)$; the co-ordinates of the dominant wavelength and $(x_i = 0.3101, y_i = 0.3162)$; the co-ordinates of the illuminant point. The color purity of present phosphor were estimated and listed in Table 6. Aforementioned results suggest that, the prepared LaOF: Tb^{3+} (1–5 mol%) nanophosphor quite useful for cool green phosphor for solid state and LED's applications.

4. Conclusions

In summary, LaOF: Tb^{3+} (1–5 mol%) nanophosphors were synthesized by ultrasound assisted sonochemical route using *EGCG* surfactant. The PXRD results confirm the high crystallinity and single tetragonal phase. The crystallite sizes of prepared samples were estimated by using both Scherrer's relation and W-H plots. From DR spectra, direct energy band gap was estimated and found to be ~5.63 eV to 5.88 eV. PALS and DB spectroscopy results reveal that the presence of cluster vacancy in the host matrix was occupied by Tb^{3+} ions. Lifetime component τ_1 is short as compared to component τ_2 due to annihilation of positrons on the grain and grain boundaries. Further, the PL intensity was found to be increased with the reduction of lattice defects. The spectroscopic investigations, bonding behavior of Tb^{3+} ions in LaOF host and the photometric characteristics indicate that the phosphor exhibit efficient green light emission and as a result it may be used as a promising green phosphor material suitable for solid state lighting and display devices when coupled with UV or blue LED.

Acknowledgement

Appendix A. Supplementary data

Supplementary data associated with this article can be found, in the online version, at http://dx.doi.org/10.1016/j.mseb.2017.07.001.

References

[1] T. Wen, Y. Zhou, Y. Guo, C. Zhao, B. Yang, Y. Wang, Color-tunable and single-band red upconversion luminescence from rare-earth doped Vernier phase ytterbium oxyfluoride nanoparticles, J. Mater. Chem. C 4 (2016) 684–690.
[2] X. Zhao, S. He, M.C. Tan, Design of infrared-emitting rareearth doped nanoparticles and nanostructured composites, J. Mater. Chem. C 4 (2016) 8349–8372.
[3] S. Al-waisawy, W.M. Jadwisienczak, J.T. Wright, D. Pendrill, F. Rahman, Laser excitation of red, green, blue and trichromatic white rare-earth phosphors for solid-state lighting applications, J. Lumin. 169 (2016) 196–203.
[4] Annemarie Nadort, Jiangbo Zhao, Ewa M. Goldys, Lanthanide upconversion luminescence at the nanoscale: fundamentals and optical properties, Nanoscale 8 (2016) 13099–13130.
[5] Enrico Bovero, Frank C.J.M. van Veggel, Conformational characterization of Eu^{3+}-doped LaF$_3$ core−shell nanoparticles through luminescence anisotropy studies, J. Phys. Chem. C 111 (12) (2007) 4529–4534.
[6] P. Dimple, Dutta, Mainak Roy, A.K. Tyagi, Dual function of rare earth doped nano Bi$_2$O$_3$: white light emission and photocatalytic properties, Dalton Trans. 41 (2012) 10238–10248.
[7] Chantal Lorbeer, Anja-Verena Mudring, White light-emitting single phosphors via triply doped LaF$_3$ nanoparticles, J. Phys. Chem. (2013), http://dx.doi.org/10.1021/jp312411f.
[8] M. Chandrasekhar, H. Nagabhushana, S.C. Sharma, K.H. Sudheer Kumar, N. Dhananjaya, D.V. Sunitha, C. Shivakumara, B.M. Nagabhushana, Particle size, morphology and color tunable ZnO:Eu^{3+} nanophosphors via plant latex mediated green combustion synthesis, J. Alloys Compd. 584 (2014) 417–424.
[9] S.C. Ramachandra Naik, H. Prashantha, S.C. Nagabhushana, H.P. Sharma, K.S. Anantha Nagaswarupa, B.M. Raju, H.B. Nagabhushana, K.M. Girish Premkumar, A single phase, red emissive Mg$_2$SiO$_4$:Sm^{3+} nanophosphor prepared via rapid propellant combustion route, Spectrochim. Acta, Part A 140 (2015) 516–523.
[10] C.J. Shilpa, N. Dhananjaya, H. Nagabhushana, S.C. Sharma, C. Shivakumara, K.H. Sudheerkumar, B.M. Nagabhushana, R.P.S. Chakradhar, Gd$_{1.96x}$Y$_x$Eu$_{0.04}$O$_3$ (x = 0.0, 0.49, 0.98, 1.47, 1.96 mol%) nanophosphors: propellant combustion synthesis, structural and luminescence studies, Spectrochim Acta, Part A 128 (2014) 730–739.
[11] J.S. Kim, P.E. Jeon, Y.H. Park, J.C. Choi, H.L. Park, G.C. Kim, T.W. Kim, White-light generation through ultraviolet-emitting diode and white-emitting phosphor, Appl. Phys. Lett. 85 (2004) 3696.
[12] P.L. Li, Z.P. Yang, Z.J. Wang, Q.L. Guo, White-light-emitting diodes of UV-based Sr$_3$Y$_2$(BO$_3$)$_4$:Dy^{3+} and luminescent properties, Mater. Lett. 62 (2008) 1455–1457.
[13] Q.Y. Zhang, C.H. Yang, Y.X. Pan, Enhanced white light emission from GdAl$_3$(BO$_3$)$_4$: Dy^{3+}, Ce^{3+} nanorods, Nanotechnology 18 (2007) 145602.
[14] C.K. Chang, T.M. Chen, Sr$_3$B$_2$O$_6$: Ce^{3+}, Eu^{2+}: a potential single-phased white-emitting borate phosphor for ultraviolet light-emitting diodes, Appl. Phys. Lett. 91 (2007) 081902.
[15] J.K. Park, M.A. Lim, C.H. Kim, H.D. Park, J.T. Park, S.Y. Choi, White light-emitting diodes of GaN-based Sr$_2$SiO$_4$: Eu and the luminescent properties, Appl. Phys. Lett. 82 (2003) 683.
[16] N. Dhananjaya, C. Shivakumara, Rohit Saraf, H. Nagabhushana, Red-emitting LaOF: Eu^{3+} phosphors: Synthesis, structure and their Judd-Ofelt analysis for LED applications, Mater. Res. Bull. 75 (2016) 100–109.
[17] L. Armelao, G. Bottaro, L. Bovo, C. Maccato, M. Pascolini, C. Sada, E. Soini, E. Tondello, Luminescent properties of Eu-doped lanthanum oxyfluoride sol–gel thin films, J. Phys. Chem. C 133 (2009) 14429–14434.
[18] A.V. Thorat, T. Ghoshal, J.D. Holmes, P.M.G. Nambissan, M.A. Morris, A positron annihilation spectroscopic investigation of europium-doped cerium oxide nanoparticles, Nanoscale 6 (2014) 608–615.
[19] S. Ghosh, G.G. Khan, K. Mandal, S. Thapa, P.M.G. Nambissan, Positron annihilation studies of vacancy-type defects and room temperature ferromagnetism in chemically synthesized Li-doped ZnO nanocrystals, J. Alloys Compd. 590 (2014) 396–405.
[20] A.Z.M.S. Rahman, Z. Li, X. Cao, B. Wang, L. Wei, Q. Xu, K. Atobe, Positron annihilation study of vacancy-type defects in fast-neutron-irradiated MgO·nAl$_2$O$_3$, Nucl. Instrum. Methods Phys. Res. Sect. B 335 (2014) 70–73.
[21] S.K. Sharma, P.K. Pujari, K. Sudarshan, D. Dutta, M. Mahapatra, S.V. Godbole, O. D. Jayakumar, A.K. Tyagi, Positron annihilation studies in ZnO nanoparticles, Solid State Commun. 149 (2009) 550–554.
[22] K. Chakraborty, A. Bisoi, B.N. Ganguly, V. Grover, A.K. Tyagi, Structural transition in rare earth doped zirconium oxide: a positron annihilation study, Mater. Res. Bull. 47 (2012) 3660–3664.
[23] A. Das, A.C. Mandal, S. Roy, P. Prashanth, P.M.G. Nambissan, Synthesis and characterization of magnesium oxide nanocrystallites and probing the

vacancy-type defects through positron annihilation studies, Physica E 83 (2016) 389–397.

[24] T. Selvalakshmi, S. Sellaiyan, A. Uedono, A.C. Bose, Investigation of defect related photoluminescence property of multicolour emitting Gd$_2$O$_3$:Dy^{3+} phosphor, RSC Adv. 4 (2014) 34257–34266.

[25] J. Yanga, T. Zhanga, L.A. Hana, X.Z. Cao, R.S. Yu, B.Y. Wang, The ability of the Coincidence Doppler Broadening Spectroscopy to characterize polymers containing different chemical elements, Spectrochim. Acta Part A 177 (2017) 97–103.

[26] M. Stadlbauer, C. Hugenschmidt, K. Schreckenbach, d P. B oni, Investigation of the chemical vicinity of crystal defects in ion-irradiated Mg and AZ31 with coincident Doppler broadening spectroscopy, PACS numbers: 78.70.Bj, 61.80.-x.

[27] Satya N. Guin, Swastika Banerjee, Dirtha Sanyal, Swapan K. Pati, Kanishka Biswas, Origin of the order-disorder transition and the associated anomalous change of thermopower in AgBiS$_2$ nanocrystals: a combined experimental and theoretical study, Inorg. Chem. 55 (12) (2016) 6323–6331.

[28] S. Seidlmayer, I. Buchberger, M. Reinerc, T. Gigl, R. Gilles, H.A. Gasteiger, C. Hugenschmidt, First-cycle defect evolution of Li$_{1-x}$Ni$_{1/3}$Mn$_{1/3}$Co$_{1/3}$O$_2$ lithium ion battery electrodes investigated by positron annihilation spectroscopy, J. Power Sources 336 (2016) 224–230.

[29] S. Jin, P. Zhang, E. Lu, L. Guo, B. Wang, X. Cao, Correlation between Cu precipitates and irradiation defects in Fe–Cu model alloys investigated by positron annihilation spectroscopy, Acta Mater. 103 (2016) 658–664.

[30] S.K. Gupta, K. Sudarshan, P.S. Ghosh, A.P. Srivastava, S. Bevara, P.K. Pujaria, R.M. Kadama, Role of various defects in the photoluminescence characteristics of nanocrystalline Nd$_2$Zr$_2$O$_7$: an investigation through spectroscopic and DFT calculations, J. Mater. Chem. C 4 (2016) 4988–5000.

[31] M. Hasegawa, Z. Tang, Y. Nagai, T. Nonaka, K. Nakamur, Positron lifetime and coincidence Doppler broadening study of vacancy-oxygen complexes in Si: experiments and first-principles calculations, Appl. Surf. Sci. 194 (2002) 76–83.

[32] S.K. Gupta, K. Sudarshan, P.S. Ghosh, A.P. Srivastava, S. Bevara, P.K. Pujari, R.M. Kadam, Role of various defects in the photoluminescence characteristics of nanocrystalline Nd$_2$Zr$_2$O$_7$: an investigation through spectroscopic and DFT calculations, J. Mater. Chem. C 4 (2016) 4988–5000.

[33] K.K. Deb, R.G. Buser, C.A. Morrison, R.P. Leavitt, Crystal fields and intensities of triply ionized rare-earth ions in cubic lanthanum oxyfluoride: an efficient ^{4}F$_{3/2}$ → ^{4}I$_{9/2}$ LaOF: Nd laser, J. Opt. Soc. Am. 71 (1981) 1463.

[34] Y.P. Du, Y.W. Zhang, Z.G. Yan, L.D. Sun, C.H. Yan, Highly luminescent self-organized sub-2-nm EuOF nanowires, J. Am. Chem. Soc. 131 (2009) 16364–16365.

[35] Y. Zhang, X.J. Li, D.L. Geng, M.M. Shang, H.Z. Lian, Z.Y. Cheng, J. Lin, Cryst. Eng. Comm. 16 (2014) 2196.

[36] M.M. Shang, D.L. Geng, X.J. Kang, D.M. Yang, Y. Zhang, J. Lin, Hydrothermal derived LaOF: Ln^{3+} (Ln = Eu, Tb, Sm, Dy, Tm, and/or Ho) nanocrystals with multicolor-tunable emission properties, Inorg. Chem. 51 (2012) 11106–11116.

[37] Y. Zhang, X.J. Kang, D.L. Geng, M.M. Shang, Y. Wu, X.J. Li, H.Z. Lian, Z.Y. Cheng, J. Lin, Highly uniform and monodisperse GdOF: Ln 3+(Ln = Eu, Tb, Tm, Dy, Ho, Sm) microspheres: hydrothermal synthesis and tunable-luminescence properties, Dalton Trans. 42 (2013) 14140.

[38] Holsa, IR-and Raman-active normal vibrations of rare earth oxyfluorides, REOF; RE = Y, La, and Gd, J. Spectrochim. Acta Part A 49 (1993) 465–470.

[39] M. Shang, D. Geng, X. Kang, D. Yang, Y. Zhang, J. Lin, Hydrothermal derived LaOF:Ln^{3+} (Ln = Eu, Tb Sm, Dy, Tm, and/or Ho) nanocrystals with multi color tunable emission properties, Inorg. Chem. 51 (2012) 11106–11116.

[40] T. Grzyb, S. Lis, Structural and spectroscopic properties of LaOF: Eu^{3+} nanocrystals prepared by the sol–gel pechini method, Inorg. Chem. 50 (2011) 8112–8120.

[41] D. Barreca, A. Gasparotto, C. Maragno, E. Tondello, E. Bontempi, L.E. Depero, C. Sada, CVD of lanthanum oxyfluoride-based thin films from a lanthanum β-diketonate diglyme precursor, Chem. Vapor. Depos. 11 (2005) 426–432.

[42] T. Grzyb, M. Wecławiak, T. Pe dzinski, S. Lis, Synthesis, spectroscopic and structural studies on YOF LaOF and GdOF nanocrystals doped with Eu^{3+} synthesized via stearic acid method, Opt. Mater. 35 (2013) 2226–2233.

[43] N. Rakov, S.A. Vieira, Q.P.S. Silva, G.S. Maciel, Facile fabrication of Eu^{3+}-doped lanthanum oxyfluoride powders by combustion processes and temperature analysis of its fluorescence for thermal sensor application, Sens. Actuators B: Chem. 209 (2015) 407–412.

[44] R.B. Basavaraj, H. Nagabhushana, B. Daruka Prasad, G.R. Vijayakumar, Zinc silicates with tunable morphology by surfactant assisted sonochemical route suitable for NUV excitable white light emitting diodes, Ultrason. Sonochem. 34 (2017) 700–712.

[45] K.S. Suslick, S.J. Doktycz, Advances in Sonochemistry, vol. 1, in: T.J. Mason (Ed.), JAI Press, New York, 1990, p. 197.

[46] K.S. Suslick, Sonochemistry, Science. 247 (1990) 1439.

[47] Mandeep Singh Bakshi, How surfactants control crystal growth of nanomaterials, Cryst. Growth Des. 16 (2016) 1104–1133.

[48] Saskia A.B.E. Van Acker, Dirk-jan Van Den Berg, MichÈl N.J.L. Tromp, Désirée H. Griffioen, Wout P. Van Bennekom, Wim J.F. Van Der Vijgh, Aalt Bast, Structural aspects of antioxidant activity of flavonoids, Free Rad Biol. Med. 20 (1996) 331–342.

[49] G.P. Darshan, H.B. Premkumar, H. Nagabhushana, S.C. Sharma, B. Daruka Prasad, S.C. Prashantha, Neodymium doped yttrium aluminate synthesis and optical properties–a blue light emitting nanophosphor and its use in advanced forensic analysis, Dye Pig. 134 (2016) 227–233.

[50] H.J. Amith Yadav, B. Eraiah, H. Nagabhushana, G.P. Darshan, B. Daruka Prasad, S.C. Sharma, H.B. Premkumar, K.S. Anantharaju, G.R. Vijayakumar, Facile ultrasound route to prepare micro/nano superstructures for multifunctional applications, ACS Sustainable Chem. Eng. (2017), http://dx.doi.org/10.1021/acssuschemeng.6b01693.

[51] H. Nagabhushana, R.B. Basavaraj, B. Daruka Prasad, S.C. Sharma, H.B. Premkumar, G.R. Vijayakumar Udayabhanu, Facile EGCG assisted green synthesis of raspberry shaped CdO nanoparticles, J. Alloys compd. 669 (2016) 232–239.

[52] K.N. Venkatachalaiah, H. Nagabhushana, G.P. Darshan, R.B. Basavaraj, B. Daruka Prasad, S.C. Sharma, Blue light emitting Y$_2$O$_3$:Tm^{3+} nanophosphors with tunable morphology obtained by bio-surfactant assisted sonochemical route, Spec. Chim. Acta Part A: Mol. Biomol. Spec. (2017), http://dx.doi.org/10.1016/j.saa.2017.04.033.

[53] A. Das, A.C. Mandal, S. Roy, P. Prashanth, S.I. Ahamed, S. Kar, M.S. Prasad, P.M.G. Nambissan, Physica E 83 (2016) 389–397.

[54] Z. Tang, T. Rewcharoon, Y. Nagai, M. Hasegawa, Acta Mater. 58 (2010) 1868–1875.

[55] M. Chowdhury, S.K. Sharma, Spectroscopic behavior of Eu^{3+} in SnO$_2$ for tunable red emission in solid state lighting devices, RSC Adv. 5 (2015) 51102–51109.

[56] R.B. Basavaraj, H. Nagabhushana, B. Daruka Prasad, S.C. Sharma, S.C. Prashantha, B.M. Nagabhushana, A single host white light emitting Zn$_2$SiO$_4$: Re^{3+} (Eu, Dy, Sm) phosphor for LED applications, Optik 126 (2015) 1745–1756.

[57] C. Suresh, H. Nagabhushana, G.P. Darshan, R.B. Basavaraj, B. Daruka Prasad, S.C. Sharma, M.K. Sateesh, J.P. Shabaaz Begum, Lanthanum oxyfluoride nanostructures prepared by modified sonochemical method and their use in the fields of optoelectronics and biotechnology, Arabian J. Chem. (2017), http://dx.doi.org/10.1016/j.arabjc.2017.03.006.

[58] M. Dhanalakshmi, H. Nagabhushana, G.P. Darshan, R.B. Basavaraj, B. Daruka Prasad, Sonochemically assisted hollow/solid BaTiO$_3$:Dy^{3+} microspheres and their applications in effective detection of latent fingerprints and lips prints, J. Sci: Adv. Mater. Devices 2 (2017) 22–33.

[59] G.P. Darshan, H.B. Premkumar, H. Nagabhushana, S.C. Sharma, B. Daruka Prasad, S.C. Prashantha, R.B. Basavaraj, Superstructures of doped yttrium aluminates for luminescent and advanced forensic investigations, J. Alloys Compd. 686 (2016) 577–587.

[60] B.P. Maheshwary, J. Singh, R.A. Singh, Singh, Luminescence properties of Eu^{3+}-activated SrWO$_4$ nanophosphors - concentration and annealing effect, RSC Adv. 4 (2014) 32605–32621.

[61] G.P. Darshan, H.B. Premkumar, H. Nagabhushana, S.C. Sharma, S.C. Prashantha, B. Daruka, Prasad, Effective fingerprint recognition technique using doped Yttrium aluminate nanophosphor material, J. Colloid Interface Sci. 464 (2016) 206–218.

[62] R.B. Basavaraj, H. Nagabhushana, G.P. Darshan, B. Daruka Prasad, S.C. Sharma, K.N. Venkatachalaiah, Ultrasound assisted rare earth doped Wollastonite nanopowders: Labeling agent for imaging eccrine latent fingerprints and cheiloscopy applications, J. Ind. Eng. Chem. 51 (2017) 90–105.

[63] B.R. Judd, Optical absorption intensities of rare-earth ions, Phys. Rev. 127 (1962) 750–761.

[64] G.S. Ofelt, Intensities of crystal spectra of rare-earth ions, J. Chem. Phys. 37 (1962) 511–520.

[65] S. Som, S. Das, S. Dutta, H.G. Visser, M.K. Pandey, P. Kumar, R.K. Dubey, S.K. Sharma, Synthesis of strong red emitting Y$_2$O$_3$:Eu^{3+} phosphor by potential chemical routes: comparative investigations on the structural evolutions, photometric properties and Judd-Ofelt analysis, RSC Adv. 5 (2015) 70887–70898.

[66] S. Som, A. Choubey, S.K. Sharma, Luminescence studies of rare earth doped yttrium gadolinium mixed oxide phosphor, Physica B 407 (2012) 3515–3519.

[67] D. Umamaheswari, B.C. Jamalaiah, T. Sasikala, T. Chengaiah, L Rama Il-GonKim, Moorthy, Photoluminescence and decay behavior of Tb^{3+} ions in sodium fluoro-borate glasses for display devices, J. Lumi. 132 (2012) 1166–1170.

[68] T. Smith, J. Guild, The C.I.E. colorimetric standards and their use, Trans. Opt. Soc. 33 (1931) 75–134.

[69] C.S. McCamy, Correlated color temperature as an explicit function of chromaticity coordinates, Color Res. Appl. 17 (1992) 142–144.

[70] J.C. de Mello, H.F. Wittmann, R.H. Friend, An improved experimental determination of external photoluminescence quantum efficiency, Adv. Mater. 9 (1997) 230–232.

[71] K.N. Venkatachalaiah, H. Nagabhushana, G.P. Darshan, R.B. Basavaraj, B. Daruka Prasad, Novel and highly efficient red luminescent sensor based SiO$_2$@Y$_2$O$_3$:Eu^{3+}, M$^+$ (M$^+$ = Li, Na, K) composite core–shell fluorescent markers for latent fingerprint recognition, security ink and solid state lightning applications, Sens. Actu. B 251 (2017) 310–325.